Available online at www.sciencedirect.com
SCIENCE DIRECT®
International Journal of Heat and Mass Transfer 48 (2005) 1064–1075
International Journal of HEAT and MASS TRANSFER
www.elsevier.com/locate/ijhmt

Magnetic resonance imaging of water freezing in packed beds cooled from below

John G. Georgiadis *, Mahadevan Ramaswamy

Laboratory of Quantitative Visualization in Energetics, Department of Mechanical and Industrial Engineering, NSF Sci. & Tech. Center of Advanced Materials for the Purification of Water with Systems (CAMPWS), 140 MEB, 1206 W. Green Street, University of Illinois at Urbana-Champaign, Urbana, IL 61801, USA

Received 24 October 2003; received in revised form 25 September 2004
Available online 15 December 2004

Abstract

Full-field quantitative visualization of freezing interfaces requires the introduction of high resolution noninvasive methods. Magnetic resonance imaging (MRI) is a versatile tool for mapping the distribution of liquids (primarily water) in three-dimensional space, and is the only practical solution in systems that are strongly refracting or opaque to visible light. MRI is employed to visualize ice formation in water-saturated packed beds consisting of spherical beads packed in a cylindrical cavity and cooled from below. Imaging of the stagnant interstitial water is accomplished by exploiting the strong contrast in proton spin density signal between interstitial ice and liquid water. Our implementation of MRI allows fully three-dimensional reconstruction of the solidification front and adequate time resolution to quantify the freezing of pore water. The effect of pore space heterogeneity near the lateral walls of the cavity, as expressed by the ratio of bed to bead diameter, is examined with respect to the shape and propagation rate of the freezing interface. A modification of the test section also allows the study of freezing in pure water which is used for comparison. The present work demonstrates the kind of extra provisions in terms of design and choice of materials of the test section that are necessary in order to accommodate the special environment of the MRI scanner in heat transfer applications.

1. Introduction

Researchers in the fields of materials processing, fluid mechanics and heat transfer, and biotechnology are keenly interested in the development of noninvasive imaging schemes that allow the reconstruction of three-dimensional interfaces and the measurement of growth rates of evolving morphologies. The freezing (or melting) of water occupying the interstitial space of porous materials occurs in a multitude of engineered or natural systems. In applications such as thermal energy storage, natural or artificial freezing of soil, freeze desalination, food processing [1], cryopreservation and cryosurgery [2], information of the shape and evolution of the boundary separating the liquid from the solid (ice) in the pore space is necessary in order to optimize or control the process. A particularly challenging problem arises when there is little or no optical access to the test section, or when the ice mass topology can only be described by volumetric data rather than by multiple views (projections).

* Corresponding author. Address: Department of Mechanical and Industrial Engineering, 158 Mechanical Engineering Building, 1206 W. Green Street, University of Illinois at Urbana-Champaign, Urbana, IL 61801, USA. Tel.: +1 217 244 7578; fax: +1 217 333 1942.
E-mail address: georgia@uiuc.edu (J.G. Georgiadis).

0017-9310/$ - see front matter © 2004 Elsevier Ltd. All rights reserved.
doi:10.1016/j.ijheatmasstransfer.2004.09.041

Nomenclature

B_0	static magnetic field strength of superconducting MRI scanner [T]
C	specific heat [$J\,kg^{-1}\,K^{-1}$]
d	diameter of glass beads [mm]
D	diameter of cylindrical packed bed [mm]
H	height of packed bed [mm]
L	latent heat of fusion [$J\,kg^{-1}$]
Ste	Stefan number (dimensionless), $C_{MS}(T_F - T_C)/L$
t	time [s]
T	temperature [K]
x, y, z	Cartesian coordinates
Z	average distance of ice interface from cooled wall [mm]
Z^*	Z/H (dimensionless)

Greek symbols

α	thermal diffusivity [$m^2\,s^{-1}$]
ΔT	unwanted temperature rise [K]
κ	thermal conductivity [$W\,m^{-1}\,K^{-1}$]
ρ	density [$kg\,m^{-3}$]
τ	dimensionless time, Eq. (4)
ϕ	porosity
ω_0	Larmor frequency [$rad\,s^{-1}$]

Subscripts

i	initial
C	cold wall
F	ice interface
L	liquid water
LM	liquid water–glass beads mixture
S	ice
SM	ice–glass beads mixture

A standard problem is usually formulated by considering the freezing of pore water in fully-saturated packed beds consisting of randomly packed beads contained in a cavity, with one or more walls maintained at a temperature below freezing. The majority of the experimental investigations employ arrays of thermal sensors imbedded in the packed bed, or record the projection of the ice–water interface from a transparent wall, cf. [3–5]. The first approach is invasive and gives sparse data from which the mapping of the general interface is impossible. The second gives information about the interface only within a few pore sizes from the transparent wall. Yang et al. [5] examined transient freezing in a square cavity filled with glass or steel beads and water, and suddenly cooled from one side. The cavity side to bead diameter ratio was approximately 10 and the cavity was rotated so that the effect of the cold wall orientation could be studied. Experiments were performed for various orientations and the location of the ice–water interface was inferred by analyzing the area of its projection on the transparent wall. Correlations for the frozen volume as a function of time t were also given: the ice volume grows as $t^{0.62}$ for glass beads and as $t^{0.94}$ for steel beads. An interesting experiment reported by Lein and Tankin [6] exploits the Christiansen effect (described in detail in Ref. [7]) to visualize the isotherms in the liquid phase in a thin packed bed cooled from above, but the information on the solidification front is again two-dimensional. Howle et al. [8] reported a shadowgraphic study of porous Rayleigh–Bénard convection but employing this approach when the interstitial space contains ice and water is impossible because a specially constructed solid matrix was used that presents only parallel or perpendicular surfaces to optical beams. As the solid matrix itself becomes more complex, a imaging technique based on radiation that does not scatter or is absorbed on the ice–water interface like visible light is required. Magnetic resonance imaging (MRI) has become the only quantitative tool for in situ study of heat and mass transport in complex flows, cf. [7,9–15].

MRI practitioners face a number of challenges when interstitial transport involves the coupling of heat and mass transfer and more than one phase occupies the pore space. We are focusing here on the case of freezing in a cylindrical container packed with unconsolidated beads, initially fully-saturated with water and cooled from below. The objectives of the present work are to (1) to examine the problems that the MRI experimentalist faces when probing the freezing of interstitial water, and (2) study the effect of packed bed coarseness on ice production and front morphology by considering two different container/bead diameter ratios. The outline of this document is as follows: In Section 2, the specifics of the particular MRI method employed here are described, along with estimates on spatial resolution and collateral heating of the sample, followed by the details of experimental setup. In Section 3, the experimental results (qualitative and quantitative) concerning the ice front propagation are reported, and comparisons are made between measured ice thickness and the predictions of a simple model for solidification. The section concludes with recommendations for the improvement

of the MRI study of the problem. Finally, concluding remarks are given in Section 4.

2. Materials and methods

2.1. Magnetic resonance imaging (MRI)

In complex multiphase systems there are obvious limitations with imaging systems employing visible light. Magnetic resonance imaging (MRI) can be used to probe liquids whose constituent molecules have unpaired nuclear spins, such as the hydrogen (H^1) nucleus (proton) of water, cf. [16]. Unlike other penetrating modalities, MRI does not depend simply on electromagnetic radiation beam attenuation through the sample but rather on the selective interaction of radio frequency (RF) photons with nuclear spins. The spins resonate at a frequency which is proportional to the local strength of an externally imposed static magnetic field, $\omega_0 = \gamma B_0$. This magnetic field, which is of the order of a few Teslas ($1\,T = 10^4\,G$), is created in the bore of a superconducting magnet which surrounds the sample, see Fig. 1. We use here the spin-density MRI sequence where the signal intensity is proportional to the number of nuclei per unit volume. However, the principal factor determining the contrast in an MRI image is not the spatial variation of nuclear density, but the highly heterogeneous distribution of the nuclear spin-*relaxation* rates in the sample. It is precisely the difference in relaxation properties of ice and liquid water that is exploited in this work.

In the following, and in order to appreciate the constraints that MRI imposes in heat and mass transfer experiments, the exposition proceeds with the spatial encoding method (by which the spatial distribution of water is imaged), a theoretical prediction of ice–water contrast, and concludes with the description of the fabricated MRI test section. For completeness, a short list of scan (operator controlled) and intrinsic (sample dependent) parameters in a standard MRI method (multislice 2-D Fourier transform with spin echo) is given in Table 1, following Wehrli et al. [17].

Referring to Figs. 1 and 2, the spatial encoding phase employs a series of z slices obtained with 2D Fourier Transform on the x–y plane and the *spin echo* sequence. The acquisition rates are such that it becomes possible to utilize the time following sampling to sequentially excite several other z-slices at a given value of the phase-encoding gradient. This sequential excitation of adjacent slices can be repeated until the nuclei in the first slice have relaxed sufficiently (in $T1 \sim 1\,s$) to be exposed to another value of the phase-encoding gradient and be re-excited by another RF pulse. This method, represented in Fig. 2, is termed *multisection* or *interleaved multislice* imaging. Fig. 2 presents the RF excitation pulse and the

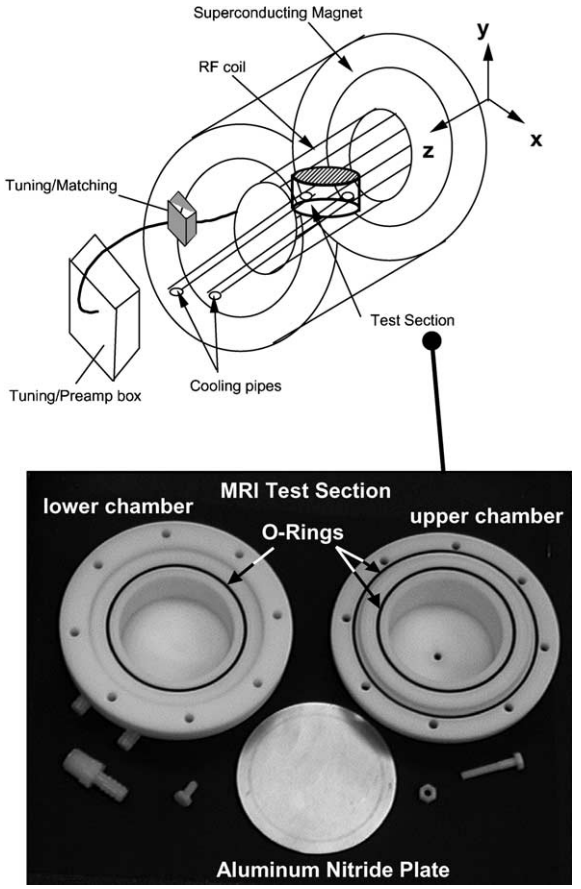

Fig. 1. MRI scanner and associated hardware, all contained in a shielded room. The field of view (FOV) can be anywhere inside the RF coil. The cooling pipes are connected to the bath/recirculator system, which is positioned as far from the magnet as possible (beyond the 5T line) in order to minimize interference. The lower panel shows the test section consisting of a cylindrical cavity (upper chamber) cooled from below by circulating coolant in the lower chamber, separated from the upper chamber by a thin AlN plate.

RF detected pulse. Interleaving in this fashion not only lowers the scan time per slice ten- to twenty-fold, but also makes any temporal scanner instabilities (over times longer than TR) equal for all slices.

The distribution of water in the whole z-slice is obtained in terms of a pixelated image. The intensity at each pixel is proportional to water concentration (averaged over the slice thickness) at the corresponding x–y coordinate. The absolute signal intensity is proportional to the number of spins that are excited in each voxel (volume element), which scales with the elementary volume $(\mathrm{FOV/NF}) \times (\mathrm{FOV/NP}) \times (\mathrm{THICK})$, hence the terminology *spin density* image. For the spin echo pulse sequence, the relative signal intensity scales

Table 1
List of operator-controlled and intrinsic parameters in a standard MRI sequence (multislice 2-D Fourier transform with spin echo)

MRI scan parameters
FOV = field of view, length or width size of the image (10 cm, 8 cm)
NP = number of phase-encoding gradients employed in the spin-warp sequence (128, 256)
One coordinate of the 2-D Fourier transform k-space
NF = number of frequency-encoding gradients, the other k-space coordinate (256, 512)
NEX = number of repetitions (excitations) of entire experiment for signal averaging (2, 1)
NSLICE = number of slices, each of thickness "THICK", obtained in multislice imaging (12, 9)
TE = echo-time between 90° pulse and the peak spin echo signal (0.02 s, 0.03 s)
TR = repetition time between 90° RF pulses (1 s, 1.33 s)

Intrinsic parameters
γ = gyromagnetic ratio, $2\pi \times 42.57 \times 10^6\,\mathrm{rad\,s^{-1}\,T^{-1}}$ for hydrogen (H^1)
$T1$ = longitudinal (spin–lattice) relaxation time
$T2$ = transverse (spin–spin) relaxation time
n = proton spin density, number of spins per unit volume of sample

The values in parenthesis correspond to the actual values used in the freezing experiments in coarse-packing (first value) and fine packing (second value) beds.

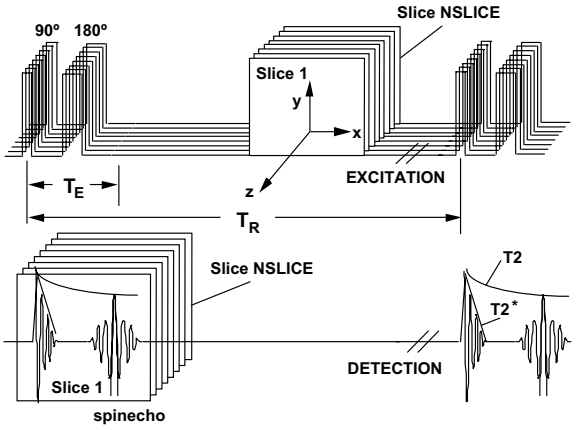

Fig. 2. RF excitation and detection during multisection imaging with spin echo. The 90° and 180° excitation RF pulses are required to encode space before the spins loose coherence (relax). $T2$ is the spin–spin relaxation time, characteristic of loss of phase coherence in the x–y plane. The signal acquisition from a stack of NSLICE z-slices is interleaved (in Fourier-space). A single Fourier-space line (corresponding to a fixed value of the phase-encoding gradient) is acquired for each z-slice.

with $n[1 - \exp\{-\mathrm{TR}/T1\}] \times \exp\{-\mathrm{TE}/T2\}$. Consequently, the contrast between two different phases of water with comparable $T1$ values, such as liquid water (subscript L) and ice (subscript S), varies as $\sim 1 - \exp\{-\mathrm{TE}/T2_\mathrm{S} + \mathrm{TE}/T2_\mathrm{L}\}$. Typically $T2_\mathrm{S} = 25\,\mu\mathrm{s}$ to 2 ms and $T2_\mathrm{L} = 50\,\mathrm{ms}$ ($T2_\mathrm{S} \ll T2_\mathrm{L}$), so there is strong contrast at the liquid water–ice interface, with a significant drop in intensity in the ice regime. On the other hand there is no MRI signal from materials without chemically identifiable protons ($n = 0$). Nevertheless, signal is received from all molecules in the field of view containing H^1, but this signal can be differentiated (in frequency space) from that emitted from the –OH group of the liquid water, since the hydrogen is bound to different chemical groups. In the case of ethylene glycol (which is used as a coolant in our experiments), signal is received from the ethylene protons but it is shifted by a 310 Hz Larmor frequency shift (*chemical shift*) from that corresponding to the –OH group of water.

In order to increase the signal-to-noise ratio, the whole experiment is also repeated NEX times and the results are averaged. The number of the total repetitions then becomes $(\mathrm{NP}) \times (\mathrm{NEX})$ which implies that the signal-to-noise ratio is also proportional to $\{(\mathrm{NP}) \times (\mathrm{NEX})\}^{1/2}$. Finally, the total scan time required is

$$T_\mathrm{tot} = (\mathrm{NEX}) \times (\mathrm{NP}) \times (\mathrm{TR}). \tag{1}$$

This is equivalent to approximately 4 min in our experiments. During this time, the test section is bathed in a static magnetic field B_0, time-varying gradient magnetic fields, and RF radiation from the sender–receiver coil. Only the RF contribution constitutes a significant thermal power input to the test section for the parameter range we employed, cf. Schaefer [18]. Starting with a quasi-static model for electromagnetic interaction between a coil with a uniform RF field and an insulated sphere of stagnant liquid water (approximating our test section), we arrive at an estimated temperature rise of only $\Delta T = 0.0027\,^\circ\mathrm{C}$. The formula employed in this calculation is [18]

$$\Delta T = \mathrm{SAR}\,\frac{T_\mathrm{tot}}{C_\mathrm{L}} \quad \text{with}$$
$$\mathrm{SAR} = \frac{\sigma \omega_0^2 B_1^2 R^2}{20\rho}\left(\mathrm{NEX} \times \mathrm{NP} \times \mathrm{NSLICE}\,\frac{\mathrm{TRF}}{T_\mathrm{tot}}\right) \tag{2}$$

where SAR is the average specific absorption ratio (absorbed RF power per unit of mass), $\sigma = 1\,\mathrm{S/m}$ (a rather high estimate of the electrical conductivity of the sample), B_1 is the magnitude of circularly-polarized magnetic field corresponding to the RF pulse, R is the radius of the hypothetical sample sphere, and TRF the individual RF pulse duration. B_1 depends on the shape of the RF pulse and is inversely proportional to TRF. We assumed sinc-modulated 90° and 180° pulses in our use of (2) and the MRI parameters used in the

scanning of fine packed beds given in Table 1. The quantity in parenthesis represents the "duty cycle" of the MRI sequence, that is, the percentage of time when the RF coil irradiates the sample.

In the case of imaging immobile water in the pore space with a typical set of MRI parameters (given in Table 1), there are two main factors that could limit the spatial resolution below the value implied by the pixel number and the FOV. Both factors related to the presence of interfaces in the FOV. Owing to the creation of local magnetic susceptibility gradients, air–water interfaces generate MRI artifacts, cf. Bakker et al. [19]. Before performing the MRI experiments, we try to eliminate all air bubbles from the area of interest. To prevent other susceptibility mismatch areas, we opted for materials of comparable magnetic properties. Solid–water interfaces on the other hand are sites of constrained water molecules (bound water) which results in reduced $T2$ times. This can be translated to *linewidth-broadening* in terms of an uncertainty, Δfreq, in the frequency domain, which is inversely proportional to $T2$. The spatial uncertainty, or limit of resolution, in the direction of an applied magnetic gradient, Grad, becomes: $2\pi\Delta\text{freq}\,(\gamma\,\text{Grad})^{-1}$. We have observed Δfreq in the range of 40 Hz for liquid water-filled packed beds constructed of glass beads. Using the typical value of Grad = 1.5 G/cm (1.5×10^{-4} T/cm), we arrive at a resolution estimate of 0.39 mm. Direct imaging of ice-air interface with MRI presents a challenging problem: in addition to the loss of signal described in the previous paragraph, spatial resolution decreases by an order of magnitude. Using a linewidth of Δfreq = 400 Hz (measured by Mizuno and Hanafusa [20]), an a priori estimate of the spatial resolution at the ice-air interface achievable with the current scanner and RF coil is about 3.9 mm.

2.2. MRI test section

The MRI experiments were performed on a horizontal bore $B_0 = 4.7$ T ($\omega_0 = 2\pi\times200\times10^6\,\text{rad}\,\text{s}^{-1}$) SISCO system located at the Biomedical Imaging Center of the University of Illinois at Urbana-Champaign. The free bore size (space available for our test section) is ultimately constrained by the internal dimensions of the RF excitation/readout coil. We used a saddle-type coil with 16.12 cm available bore diameter.

The test section essentially consists of two chambers separated by a heat exchanging surface (Fig. 1). It was designed to operate within the specifications required to freeze water inside the bore of the MRI scanner, cf. Greywall [21]. Owing to the presence of strong magnetic fields and RF radiation in MRI, ferromagnetic materials cannot be placed in or near the bore of the scanner. Therefore, the test section is constructed almost entirely from plastics, with the exception of the heat exchanging surface which is composed of aluminum nitride, a ceramic. Aluminum nitride has the advantage of relatively high thermal conductivity (one third of that of copper), poor electrical conductivity (which minimizes RF power absorption), and similar magnetic susceptibility to the rest of the test section. The cooling fluid, a mixture of ethylene glycol and water, is provided by a Neslab RTE-210 recirculating bath. The use of ethylene glycol requires that the materials used in the heat exchanger are resistant to chemical corrosion. The lower half of the test section (the shell housing the cooling fluid) is connected through 12 m of insulated Tygon™ tubing to the bath, so that the distance between the bath and the magnet is more than 5 m, which brings the susceptible bath parts (pump, electronics) within the 5–10 G range.

The shell of the test section is constructed of natural Delrin™. Delrin was selected for its good magnetic properties, corrosion resistance, hardness and ease of machinability. The outer dimensions of the test section are restricted by the inner diameter of the imaging RF coil (refer to Fig. 1). There are two separate chambers in the test section. Cooling fluid from the bath circulates in the lower chamber. The upper chamber is a cylindrical cavity with 12.7 mm thick walls, with inner dimensions of $H = 40.26$ mm (height) and $D = 76.2$ mm (diameter), and a chimney-like opening on top for venting and allowing the water to escape during freezing. It houses the sample: a solid matrix consisting of a packed bed of glass beads fully-saturated with water. The two chambers are divided by a circular disk of 108 mm-diameter aluminum nitride which forms the heat exchange surface between the ethylene glycol and the sample. The thickness of the aluminum nitride plate is 1 mm (0.040 in.). This thickness choice allows rapid heat exchange between the two chambers, while at the same time maintaining enough structural integrity to prevent failure of the plate due to any pressure differences between the upper and lower chambers. Two nitrile O-rings, one on each side of the aluminum nitride plate, form the seal that prevents leakage from either chamber. An extra O-ring is fitted directly between the two flanges of Delrin to prevent fluid leaking to the scanner in case either of the interior O-rings fails. The upper chamber contains three nylon plugs, which can be fitted with fiberoptical thermometry probes to monitor the temperature in selected locations inside the upper chamber. During the coarse-packing experiment discussed below, a fiberoptical thermometer lead was attached on the aluminum nitride plate, on the side of the packed bed, and another probe was monitoring the temperature of the coolant. The first probe was proven too intrusive during the freezing of the packed beds consisting of fine beads and was removed. Finally, the whole test section is thermally insulated by enclosing it in a jacket made of a 2 cm thick sheet of insulation.

3. Experimental results and discussion

3.1. Experimental protocol and pore space reconstruction

MRI can capture the phenomenon of freezing in a fully saturated porous medium by allowing the visualization of progressive stages of the liquid–solid interface. In our experiments, only liquid water gives significant MRI signal because the relaxation time $T2$ of ice is very short (see discussion in Section 2). The test section was positioned in the scanner so that the cold plate was horizontal and the sample was cooled from below. The upper chamber was filled with uniform glass beads and completely saturated with de-aerated water. Two sets of packed beds were used: a coarse-packing with $d = 14$ mm beads, and a fine-packing with $d = 3$ mm beads. For the coarse packing, MRI acquisition was performed in a series of transient experiments in which the bath and the plate were left to reach thermal equilibrium at -1 °C, and then the bath thermostat was set to a low temperature. The plate would then cool down slowly, owing to the large thermal mass of the coolant in the bath and the 10 m of tubing. Fig. 3 gives the transient behavior of the bath temperature and the temperature at the aluminum nitride cold plate surface (packed bed side) as measured with the fiber-optical thermometer, as well as the average height of ice in the test section obtained via image processing the MRI scans. For the fine packing, the test section was imaged as it cooled down starting from 22 °C (room temperature) and reaching approximately -8 °C. This temperature was obtained by a standard thermocouple on the same apparatus and cooling bath settings but *outside* the MRI scanner. For comparison, data from a pure water freezing experiment, described after the subsequent packed bed subsections, are also included in Fig. 3.

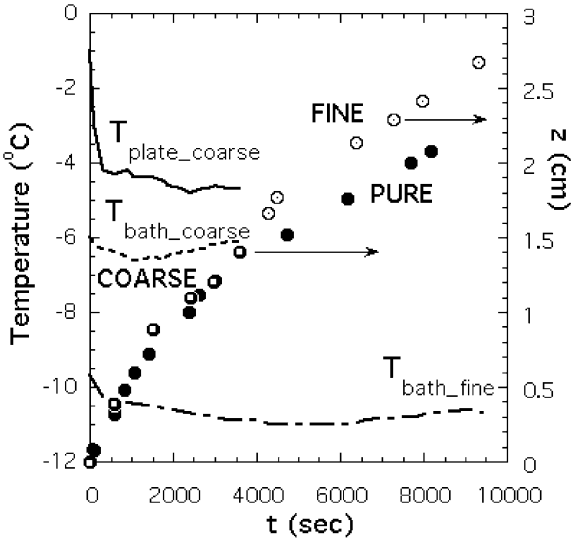

Fig. 3. The evolution of average height of freezing front, cooling bath and cold plate temperature as a function of time. The experimental data for height are represented by solid circles (pure water), open circles (fine packed bed), and ringed circles (coarse packed bed). The small increase in the coarse-packing plate temperature corresponds to latent heat release during freezing.

The first coarse-packing imaging experiment consisted of six consecutive MRI scans. Each scan produced a set of twelve 2-D horizontal slices normal to the vertical axis of the test section, which corresponds to the vertical axis y of Fig. 1. The slices are positioned 0.5 cm apart to span the entire inner volume of the upper chamber which contains the packed bed. The image of each slice contains 256×128 pixels, corresponding to a field of view of 10×10 cm. The visualization of the 3D matrix of packed beads contained in the MRI test section, before the onset of freezing, was used to assess the accuracy of the MRI data in recreating volumes. First, the beads' cross sections were recreated by digitally enhancing the glass–water interface of the MRI slices and the whole packed bed was reconstructed as a 3D object by interpolating between the slices. Second, the pore space was directly measured by emptying the test section, counting the beads, and computing their volume. Comparison between the MRI-measured ($\phi = 0.50$) and the directly-measured ($\phi = 0.49$) pore space volumes gives a 2% volumetric error. There was no appreciable distortion (deviation from sphericity) for the beads at this level of resolution. The porosity of the fine-packing bed ($\phi = 0.42$) was estimated by weighing a known quantity of the 3 mm beads, then weighing the whole sample contained in the cavity, estimating the total quantity and computing its volume (since we have monodisperse spherical beads), and finally subtracting from the known cavity volume. In our modeling discussed in the next section, we use $\phi = 0.49$ for the coarse and $\phi = 0.40$ for the fine-packing beds.

In an earlier phase of this investigation [22], the bath was not placed sufficiently far from the scanner, so each MRI scan obtained with the multislice sequence resulted in approximately $\Delta T = 1.52$ °C–2 °C temperature increase in both bath and on the aluminum nitride plate (measured immediately after each scan). As the a priori estimate of Eq. (2) in Section 2 indicates, RF thermal input in our settings can be only 0.0027 °C. This estimate was checked against an upper limit obtained on the basis of the RF transmitter power (applied to the RF coil and adjusted by the operator to produce the 90° and 180° pulses). Indeed, the delivered energy during the $T_{tot} = 341$ s for the NSLICE = 9 fine-packing experiment was 24.12 J. This implies that the temperature of a water sphere of radius 0.038 m would be raised by 0.015 °C at most. This is consistent with the a priori estimate because not all power applied to the RF coil is absorbed

by the sample. So, it became certain that RF heating did not cause the temperature rise, but that the electromagnetic influence of the scanner was severe enough to relax the temperature control of the bath. Fast switching magnetic fields (generated during the MRI space encoding procedure) induce currents in conductors and thus interfere with the electronic circuit of the thermostat during scanning. This interference was eliminated by placing the thermostatic bath behind the 5G line in subsequent runs.

3.2. Ice front reconstruction in coarse-packing bed

The liquid water-saturated pore space has been volumetrically recreated from one scan during freezing and is given in Fig. 4(a). The top is truncated above a horizontal slice in order to visualize the spherical cavities corresponding to the spherical beads (glass beads are not visible in MRI). Similar cavities are also distributed in the interior of the truncated cylindrical volume (as the cut-out in Fig. 4(a) demonstrates). The prominent trench visible on the top marks the presence of an air bubble which is trapped under the upper wall of the cavity. During subsequent experiments, care was taken to eliminate such bubbles by tilting and shaking the sample, and verifying via MRI the absence of such odd-shaped cavities.

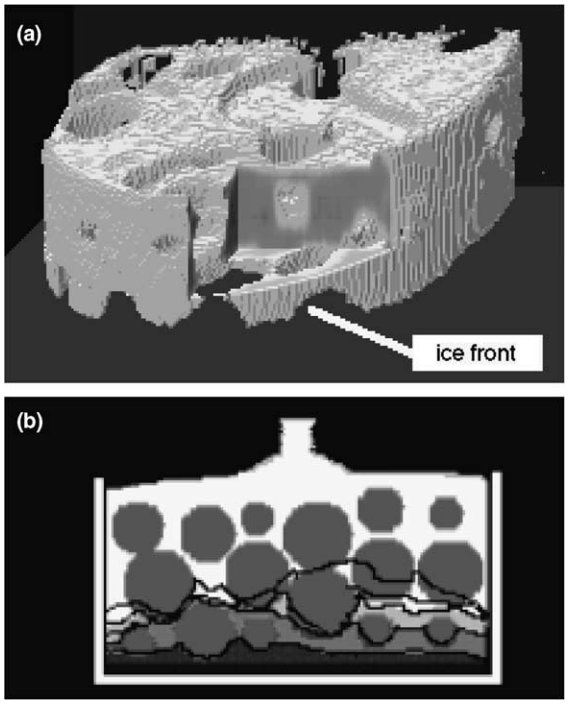

Fig. 4. MRI spin density images of freezing in coarse packed bed ($D/d = 6$). (a) Volumetric reconstruction of the interstitial liquid water. (b) Time evolution of the liquid–solid interface. The gray disks are the cross-sections of glass beads, white denotes liquid water. Each image corresponds to the same vertical slice near the axis of the cylindrical test section. The front profiles (solid lines) are obtained at 10 min, 25 min, 40 min, 50 min, and 60 min after the freezing inception.

The second set of coarse-packing experiments, the results of which are presented in Fig. 3 and will be further discussed below, was composed of six MRI scans, each revealing a different position of the freezing front. Each scan corresponds to a set of twelve 2-D vertical slices, with each slice containing 256×128 pixels and positioned normal to the z axis shown in Fig. 1. The slices are 0.5 cm apart, creating a 6 cm-thick stack containing $256 \times 128 \times 12$ voxels. This experiment involves vertical sectioning (normal to the front) which allows increased resolution of the solidification front, and permits the reconstruction of the solid–liquid interface as a function of time and space. Each scan required approximately 4 min. A composite image is given in Fig. 4(b), consisting of the position of the freezing interface in the central slice (cross-section containing the vertical axis of the cylinder) at different times. From this figure, we can infer that the general shape of the interface becomes increasingly convex as the front propagates upwards.

Using the total data set (12 slices), the volume of ice (including the glass beads it encloses) is estimated. The average height of the frozen column, which is bounded by the aluminum nitride plate from below and by the water–ice front from above, is computed by integrating the MRI slices and is given in Fig. 3. This averaging is accomplished by summing up the volume of the water-filled voxels, subtracting it from the cavity volume and dividing the result by the area of the bottom cavity wall. Based on the measured front speed, the ice interface moves an average 1.6 mm during each 4 min MRI scan. This is effectively the spatial resolution of the ice–water front owing to motion "blurring"; this resolution may be juxtaposed to the a priori estimate of 0.39 mm at the ice–glass interface (based on linewidth-broadening) and a pixel resolution in the range of 0.39–0.156 mm (based on the field of view given in Table 1).

3.3. Ice front reconstruction in fine-packing bed

The progression of the ice–water interface in the $d = 3$ mm packed bed is similarly tracked with MRI. Fig. 3 depicts the average interface height as a function of time, starting from $t = 0$ when the onset of freezing was estimated to have occurred, superimposed on the bath temperature record. Contrary to the coarse bed experiments, a variable number of vertical slices was acquired during each MRI scan, each resulting to a different temperature rise. The first two data points were acquired with a single slice scan, the fourth with NSLICE = 5, and the third and fifth with NSLICE = 9. Fig. 5(a) gives the time evolution of the solid–liquid

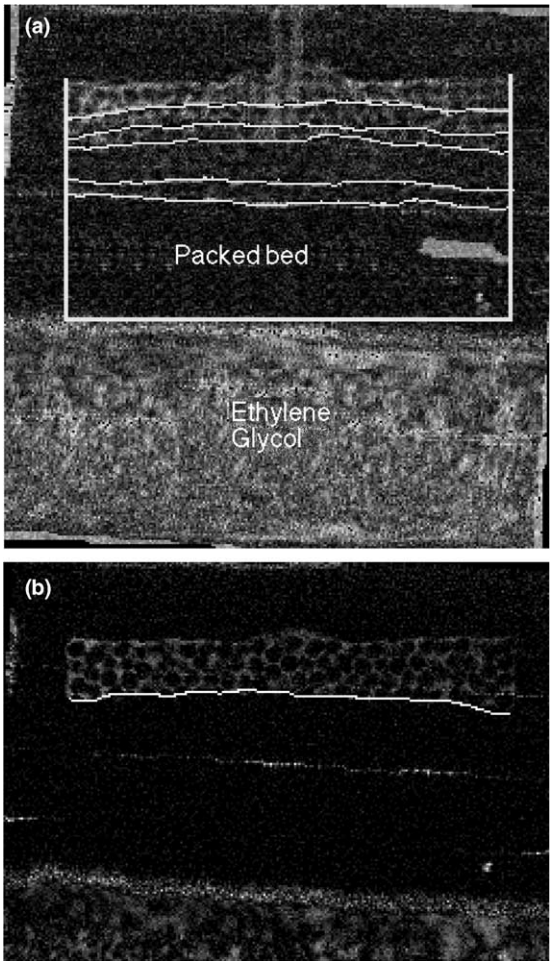

Fig. 5. MRI spin density images of freezing in fine packed bed ($D/d = 25$). (a) Time evolution of the liquid–solid interface during freezing in the case when a packing defect developed. Image is obtained by superimposing the central cross section and the front profiles (white lines added during post-processing) are obtained at 53 min, 70 min, 101 min, 113 min, 133 min, and 155 min after the freezing inception. The noisy pattern below the packed bed originates from motion artifacts in the flowing water–ethylene glycol mixture (coolant). (b) The liquid–solid interface at 158 min after inception, from the experimental run that corresponds to open circle the data of Fig. 3.

interface during freezing, by superposing the slice containing the vertical axis of the cavity. It is clear that the ice–water interface remains much flatter than the coarse-packing case. During early scans, a water-filled cavity appeared near the right boundary, probably caused by presence of the fiberoptic thermometer in the interstitial space, causing a shifting of the beads and the creation of a lens-like pore in that area. After the experiment was repeated without placing a probe inside the packed bed, this problem disappeared and the contrast in the frozen section of the MRI images became uniform. Fig. 5(b) corresponds to last data point shown in Fig. 3: the location of the water–ice front is marked by the white line and there are no packing defects.

3.4. Ice front reconstruction in pure water

In order to generate a reference freezing experiment, the upper chamber cavity was modified to allow the freezing of pure water in the absence of a packed bed. During preliminary experiments, we observed that the absence of a solid matrix, the cooling nonuniformity at the lower plate and the lowering of the water density upon freezing resulted in the destabilization of the ice layer formed and the onset of weak natural convection in the pure water pool. To "anchor" the ice column in the cavity and to create conditions favorable to one-dimensional freezing in the bulk, a thin solid frame was inserted in the upper chamber as shown in Fig. 6(a). It consists of a 4×4 lattice assembled of

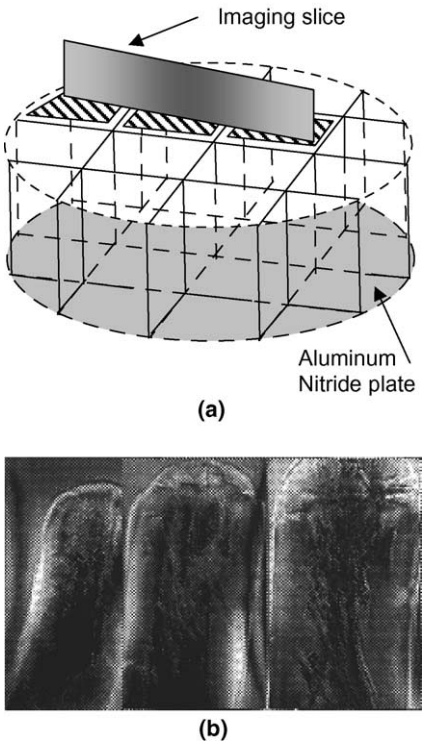

Fig. 6. Setup for freezing and MRI visualization of pure water. (a) Schematic of 4×4 separating lattice made of 2 mm-thick borosilicate glass and sandwiched between the bottom and top plates of the upper chamber in the test section depicted in Fig. 1. The lattice divides the cylindrical cavity into 16 vertical channels. (b) Detail of high-resolution MRI image of ice column growing in three adjacent channels obtained on the imaging slice shown in (a). The image width corresponds to 25 mm.

1 mm-thick borosilicate glass plates positioned vertically and spanning the distance between the bottom and top plates of the upper chamber. The lattice divides the cylindrical cavity into 16 vertical channels. Given the thinness of the lattice, this configuration essentially corresponds to the limit $\phi \to 1$ ("pure" water). Freezing experiments were conducted with the parameters (initial bulk temperature and lower plate supercool) used for the fine-packing bed experiment, and the ice front was imaged with the same (interleaved multislice) MRI protocol and was reconstructed with the same voxel-counting algorithm discussed earlier. Fig. 6(b) presents a single high-resolution vertical MRI slice showing the ice columns in three neighboring channels marked by the cross-hatched areas in Fig. 6(a). The plane of the slice is also indicated in Fig. 6(a): note that the slice is not parallel to the lattice walls. The height of the ice columns decreases gradually as the outer cavity wall is reached. This trend is expected, since the thermal boundary conditions—and consequently freezing—become increasingly less uniform towards the perimeter of the cavity where heat losses occur. Finally, imaging artifacts corresponding to the difference between the magnetic susceptibility of glass and water (and possibly trapped air bubbles) are also evident along the vertical glass plates separating the three channels. Numerous crystal defects and air bubbles are also evident in the ice–water interface at the top of Fig. 6(b).

3.5. One-dimensional model for ice front propagation

The upwards movement of the ice–water interface during freezing was simulated with an one-dimensional conduction model, assuming that the water saturated packed bed is a homogeneous medium in contact with an isothermal cold plate from below and unbounded from above. It is assumed that the packed bed–water system is stably stratified and conduction is the dominant heat transfer mechanism. The fine-packing bed experiment was simulated with $T_i - T_F = 22\,^\circ\mathrm{C}$ superheat (difference between packed bed temperature and freezing point) and $T_F - T_C = 8\,^\circ\mathrm{C}$, in contrast to the $T_i - T_F = -1\,^\circ\mathrm{C}$ supercool and $T_F - T_C = 5\,^\circ\mathrm{C}$ for the coarse-packing case. The thermal properties of the solid matrix-liquid water and solid matrix-ice portions of the sample were estimated by volumetrically averaging the properties of the constituents, using the properties given in Table 2. For example, the effective conductivity of the frozen and unfrozen portions were estimated by the following formulas

$$\kappa_{SM} = \phi\kappa_S + (1-\phi)\kappa_{Glass},$$
$$\kappa_{LM} = \phi\kappa_L + (1-\phi)\kappa_{Glass} \quad (3)$$

The solution of this freezing front propagation problem (a variation of the Stefan problem) is given in Poulikakos [23] in terms of a nonlinear algebraic equation for a properly scaled distance between the front and the cold plate, which is defined as $0.5z\,(\alpha_{SM}t)^{-1/2}$. The solution of this equation was obtained for two porosities for each of the experiments: $\phi = 0.49$ and 1 (coarse-packing) and $\phi = 0.40$ and 1 (fine-packing). The results for $\phi = 1$ correspond to the freezing of pure water and are used as a control. Notice that there are two sets of curves corresponding to the different thermal conditions. The results are presented in Fig. 7, in terms of a nondimensional front height z^* versus a nondimensional time

$$\tau = \left[\frac{\alpha_L}{H^2}\frac{(T_F - T_C)}{L}C_L\right]t \quad (4)$$

Table 2
Thermophysical parameters for the components of the packed bed

	Liquid water	Ice	Borosilicate glass
Density [$\mathrm{kg\,m^{-3}}$]	1000	920	2640
Conductivity [$\mathrm{W\,m^{-1}\,K^{-1}}$]	0.569	1.88	1.09
Diffusivity [$\mathrm{m^2\,s^{-1}}$]	1.35×10^{-7}	1.0×10^{-6}	5.1×10^{-7}
Fusion latent heat [$\mathrm{J\,kg^{-1}}$]	333×10^{3}	–	–

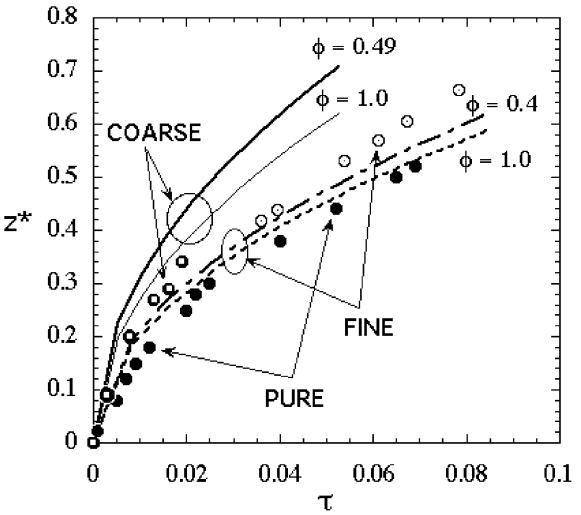

Fig. 7. Comparison between measured (circle symbols explained in caption of Fig. 3) and predicted (solid lines for coarse and dash lines for fine packed bed and pure water) average height evolution as a function of time during freezing. The theoretical predictions are obtained for two porosities (bulk and wall region) for each of the two packed beds, while the $\phi = 1$ curve for the fine bed corresponds to the pure water case.

This nondimensional time is defined slightly differently in Yang et al. [5].

There is very good agreement between theoretical estimates of height and experimental results for the pure water case, but there are noticeable disagreements for the packed bed cases. Due to the nonuniformity of random packing of the spheres near walls, the porosity is very high in an annular region of thickness 2–3d near flat walls, compared to the bulk value at the core (near the vertical axis of the cylindrical cavity). The simulation results depicted in Fig. 7 indicate that the growth of the $\phi = 0.49$ and 0.4 fronts (representing the core) is higher than that of $\phi = 1$ (representing the wall region). This is consistent with the convexity of the observed freezing front depicted in Fig. 5(b). Solidification in the core of the bed proceeds faster than its lateral surface. This "wall-effect", which is extremely pronounced in the coarse-packing bed ($D/d = 6$), affects the solidification front in the following ways: The conductivity of glass is approximately twice that of water, see Table 2. The increased thermal conductivity of the packed bed is therefore higher at the core (near the vertical axis of the cylindrical cavity) than the perimeter. Hence, the core region cools earlier. More latent heat is released (during freezing) near the walls since there is more water there. This effect is insignificant for the pure water case and less significant in the fine-packing bed case ($D/d = 25$), and again the MRI observations confirm this, cf. Figs. 5 and 6.

The solution of the Stefan problem with isothermal cooling plate yields z^* proportional to $\tau^{0.5}$. The model predictions do not reproduce quantitatively the observed front growth rates for the packed bed cases. Our experimental results can be correlated by the following power laws:

$$z^*_{\text{fine}} = 3.04\tau^{0.6}, \quad z^*_{\text{coarse}} = 5.85\tau^{0.71} \tag{5}$$

The disagreement can be attributed to the exclusion of two- and three-dimensional effects, and the adoption of a simplified thermal boundary condition on the lower boundary. Among the two model deficiencies, the latter is significantly more severe. It is clear from Fig. 3 that the bottom plate did not remain isothermal during freezing. Given the fact that the plate was convectively cooled by a thermostatically controlled bath, a convective boundary condition at the cooled wall is more appropriate. The approximate solution of Ma and Wang [24] implies that, for negligible superheat (the coarse bed experiment), the front progresses as $z^* = c_1\tau - c_2\tau^2 + \cdots$, where c_1, c_2 are constants that depend on the heat transfer coefficient between the plate and the cooling fluid. This is consistent with the measured exponent 0.71 of Eq. (5), as well as with the linear growth of the front during the first three scans for the coarse bed given in Fig. 7. The temporal behavior of the freezing front with significant superheat (fine-packing bed experiments) is more complicated. The front growth rate is slower than that for the zero superheat case, it reaches a peak value, and then decays [24]. This might account for the change of slope of the z^* versus τ curve given in Fig. 7. Finally, it is worth noting that the fine-packing bed result given in (5) agrees with the exponent 0.62 measured by Yang et al. [5], obtained with a corresponding $D/d = 10$ and similar superheat.

3.6. Recommendations for improved methodology

Increasing the spatial resolution near the ice–water interface will incur penalties in terms of longer scanning times, as the analysis in Section 2 implies. This will limit the temporal resolution which is critical in imaging evolving solidification fronts. It is worth mentioning in passing that the success of the employed MRI sequence in our experiment hinges on the fact that motion in the interstitial water as well in the bulk water above the ice front was negligible during freezing. The lower part of Fig. 5(a) gives an example of the generation of motion artifacts in the water–ethylene glycol mixture reservoir where the forced recirculation of the coolant occurs. Improved MRI sequences are necessary to compensate for flow in the field of view and to quantify the velocity field, cf. Moser et al. [12,13].

In order to improve the modeling of freezing front propagation in complex media, the pioneering work of Hong et al. [2] shows that it is feasible to couple MRI results with numerical heat transfer simulations. The freezing front boundary obtained by MRI sectioning can be used as a boundary condition for a numerical scheme (a finite-difference scheme was used in [2]) to produce the temperature field throughout the sample. The slow speed of front propagation (in our experiments, $Ste = 0.0625$ for coarse and $Ste = 0.123$ for fine-packing) reduces the heat transfer model to a quasi-steady conduction equation, which can be solved on a grid that is commensurate with the pixelated MRI field of view. This is particularly useful in imaging the ice domain which is not resolved with the MRI sequence employed here.

4. Conclusions

A novel application of a noninvasive high-resolution imaging technology, magnetic resonance imaging (MRI) has been demonstrated for the study of structure evolution in two-phase media containing ice–water interfaces. MRI relies on the interaction of radiofrequency radiation and nuclear spins in the presence of magnetic fields. We have used a multislice MRI sequence to map the freezing of water contained in a coarse and a fine packed bed cooled from below. Experiments in pure water were also used as controls. The position of the water–ice

interface was visualized indirectly, by mapping the water column in space and time. The average distance of the interface from the plate was used to quantify the solidification rate. Initially, solidification was found to progress linearly with respect to time in the case with negligible superheat, and faster than the square root of time in later stages. There is very good agreement between the one dimensional modeling of height evolution and experimental results for the pure water case, but there are noticeable disagreements for the packed bed cases. The shape of the solidification front became convex upwards during freezing in the coarse-packing bed ($D/d = 6$) owing to the wall effect, while the front inside the fine bed ($D/d = 25$) remained more uniform. A summary of the constraints of MRI, in its present implementation, is given below.

The test section and fluid needs nonferromagnetic media with low electrical conductivity. Magnetic susceptibility interface artifacts can be severe, especially near gas interfaces. What MRI lacks in spatial resolution (without special RF coils, one can routinely obtain 100 μm-wide pixels, compared to 1 μm for optical methods), it makes up in penetration depth into opaque media. In our experiments, the 390–156 μm pixels provide adequate resolution in space, and allow the reconstruction of the freezing front in time. Finally, in order to produce quantitative 3D reconstruction, MRI studies have to rely on extensive image processing and image analysis. Acquiring and analyzing 3D data (representing complex morphologies) makes high demands in terms of gigabyte-size digital storage, high resolution color displays, or video. The MRI technique has seen explosive growth in the field of biomedical imaging during the last twenty years, and has come full circle back to the applied sciences. This work serves to demonstrate that the MRI user has to be familiar with the fundamental as well the applied aspects of this very promising technology before adopting it in a specific application.

Acknowledgments

The authors would like to thank Mr. Paul Greywall for his assistance in constructing the test section, and during acquisition and image processing of some preliminary results. We gratefully acknowledge the financial support of the Department of Mechanical and Industrial Engineering, the Research Board, and the Air Conditioning and Refrigeration Center (Dr. Clark Bullard, director) of the University of Illinois at Urbana-Champaign, the National Science Foundation (grant CTS-9396252 and cooperative agreement CTS-0120978), and the Electric Power Research Institute (grant WO8034-07, Dr. Sekhar Kondepudi, monitor). Special thanks to Dr. Doug Morris and to Dr. Andrew Webb of the Biomedical Imaging Center of the University of Illinois at Urbana-Champaign (first established by Dr. Paul Lauterbur).

References

[1] L.D. Hall, T.A. Carpenter, Magnetic resonance imaging: a new window into industrial processing, Magn. Reson. Imag. 10 (1992) 713–721.
[2] J.S. Hong, S. Wong, G. Pease, B. Rubinsky, MR imaging assisted temperature calculations during cryosurgery, Magn. Reson. Imag. 12 (7) (1994) 1021–1031.
[3] J.A. Weaver, R. Viskanta, Freezing of liquid-saturated porous media, ASME J. Heat Transfer 108 (1986) 654–659.
[4] S. Chellaiah, R. Viskanta, Freezing of water-saturated porous media in the presence of natural convection: experiments and analysis, ASME J. Heat Transfer 111 (1989) 425–432.
[5] C.-H. Yang, S.K. Rastogi, D. Poulikakos, Freezing of water-saturated inclined packed bed of beads, Int. J. Heat Mass Transfer 36 (14) (1993) 3583–3592.
[6] H. Lein, R.S. Tankin, Natural convection in porous media—II. Freezing, Int. J. Heat Mass Transfer 35 (1) (1992) 187–194.
[7] S.A. Bories, M.C. Charrier-Mojtabi, D. Houi, P.G. Raynaud, Non-invasive measurement techniques in porous media, in: S. Kakaç, B. Kilkis, F.A. Kulacki, F. Arinç (Eds.), Convective Heat and Mass Transfer in Porous Media, NATO ASI vol. E 196, Kluwer, Netherlands, 1991, pp. 883–921.
[8] L.E. Howle, R.P. Behringer, J.G. Georgiadis, Visualization of convective fluid flow in a porous medium, Nature 362 (1993) 230–232.
[9] J.G. Georgiadis, Multiphase flow quantitative visualization, Appl. Mech. Rev. 47 (6) (1994) S315–S319, Part 2.
[10] M.D. Shattuck, R.P. Behringer, G.A. Johnson, J.G. Georgiadis, Convection and flow in porous media. Part 1. Visualization by magnetic resonance imaging, J. Fluid Mech. 332 (1997) 215–245.
[11] K. Ogawa, M. Tobo, N. Iriguchi, S. Hirai, K. Okazaki, Simultaneous measurement of temperature and velocity maps by inversion recovery tagging method, Magn. Reson. Imag. 18 (2000) 209–216.
[12] K.W. Moser, L.G. Raguin, J.G. Georgiadis, MRI tomographic study of helical modes in bifurcating Taylor–Couette–Poiseuille flow, Phys. Rev. E 64 (2001) 016319.
[13] K.W. Moser, L.G. Raguin, J.G. Georgiadis, Synchronized EPI phase contrast velocimetry in a mixing reactor, Magn. Reson. Imag. 21 (2003) 127–133.
[14] L.F. Gladden, P. Alexander, M.M. Britton, M.D. Mantle, A.J. Sederman, E.H.L. Yuen, In situ magnetic resonance measurement of conversion, hydrodynamics and mass transfer during single- and two-phase flow in fixed bed reactors, Magn. Reson. Imag. 21 (2003) 213–219.
[15] K.W. Moser, J.G. Georgiadis, Extraction and validation of correlation lengths from interstitial velocity fields using diffusion-weighted MRI, Magn. Reson. Imag. 22 (2004) 257–268.
[16] Z.-P. Liang, P.C. Lauterbur, Principles of Magnetic Resonance Imaging: A signal Processing Perspective, IEEE Press, 2000.

[17] F.W. Wehrli, J.R. MacFall, D. Shutts, G.H. Glover, N. Grigsby, V. Haughton, J. Johanson, The dependence of nuclear magnetic resonance (NMR) image contrast on intrinsic and pulse sequence timing parameters, Magn. Reson. Imag. 2 (1) (1984) 35–243.

[18] D.J. Schaefer, Bioeffects of MRI and Patient Safety, The Physics of MRI: 1992 AAPM Summer School Proceedings, Medical Physics Monograph No. 21, American Institute of Physics, 1992, pp. 607–646.

[19] C.J.G. Bakker, R. Bhagwandien, M.A. Moerland, M. Fuderer, Susceptibility artifacts in 2DFT spin-echo and gradient-echo imaging: the cylinder model revisited, Magn. Reson. Imag. 11 (1993) 539–548.

[20] Y. Mizuno, N. Hanafusa, Studies of surface properties of ice using nuclear magnetic resonance, J. Phys. 48 (3) (1987) C-1511–C-517.

[21] P. Greywall, Scanning confocal microscopy and magnetic resonance imaging of freezing interfaces, Masters Thesis, Mechanical and Industrial Engineering Department, University of Illinois at Urbana-Champaign, 1994.

[22] J.G. Georgiadis, M. Ramaswamy, Quantitative visualization of structure in freezing porous media via magnetic resonance imaging, Proc. 2nd European Thermal-Sci. 14th UIT Nat. Heat Transfer Conf. Rome 2 (1996) 1033–1042.

[23] D. Poulikakos, Conduction Heat Transfer, Prentice-Hall, New Jersey, 1994, Chapter 9.

[24] J. Ma, B.-X. Wang, The penetration rate of solid–liquid phase-change heat transfer interface with different kinds of boundary conditions, Int. J. Heat Mass Transfer 38 (11) (1995) 2135–2138.